

# Recursive Interferometric Surface-wave Suppression

## For Improved Reflection Imaging

Faezeh Shirmohammadi<sup>1,\*</sup>, Deyan Draganov<sup>1</sup>, Ranajit Ghose<sup>1</sup>, Eric

Verschuur<sup>1</sup> and Kees Wapenaar<sup>1</sup>

<sup>1</sup>Department of Geoscience and Engineering, Delft University of Technology, 2628 CN Delft,

The Netherlands

\*Corresponding author: [f.shirmohammadi@tudelft.nl](mailto:f.shirmohammadi@tudelft.nl)

### Abstract

High-resolution seismic reflections are essential for imaging and monitoring applications. In seismic land surveys using sources and receivers at the surface, surface waves often dominate, masking the reflections. In this study, we demonstrate the efficacy of a two-step procedure to suppress surface waves in an active-source reflection seismic dataset. First, we apply seismic interferometry (SI) by cross-correlation, turning receivers into virtual sources to estimate the dominant surface waves. Then, we perform adaptive subtraction to minimise the difference between the surface waves in the original data and the result of SI. We propose a new approach where the initial suppression results are used for further iterations, followed by adaptive subtraction. This technique aims to enhance the efficacy of data-driven surface-wave suppression through an iterative process. We use a 2D seismic reflection dataset from Scheemda, situated in the Groningen province of the Netherlands, to illustrate the technique's efficiency. A comparison between the data after recursive interferometric surface-wave suppression and the original data across time and frequency-wavenumber domains shows significant suppression of the surface waves, enhancing visualization of the reflections for following subsurface imaging and monitoring studies.

**Keywords:** Data processing, Seismic Interferometry, Seismics, Surface waves, Groningen, Reflections.

# 1. Introduction

28

Seismic data acquired on land is often contaminated by surface waves, which are a significant noise source for reflection seismic studies. The surface waves often have a velocity and frequency content similar to those of the investigated reflections, which makes it challenging to suppress them from the dataset. Conventionally, surface waves are suppressed during data processing using methods such as frequency-offset (f-x) (Yilmaz, 2001), frequency-wavenumber (f-k), or bandpass filtering. However, these approaches can prove ineffective when surface waves are scattered and overlap with the frequency and moveout of the reflected body waves that we intend to preserve. The f-k filter may result in artefacts due to signal distortion and spatial correlation of the background noise because the surface-wave energy may be distributed over a significant range of the f-k spectrum (Konstantaki et al., 2015), thus further lowering the quality of the reflections.

Recently, the prediction of surface waves with seismic interferometry (SI) and their subsequent adaptive subtraction from seismic reflection data has emerged as a technique for suppressing surface waves (Dong et al., 2006; Halliday et al., 2010). In SI, seismic observations from various receiver locations are, for example, cross-correlated to retrieve new seismic responses from virtual sources positioned at the receivers' locations. This process enables the retrieval of seismic responses between pairs of receivers. For suppression, the retrieved responses are then subtracted from the original field recordings using least-squares matching, resulting in data with suppressed surface waves. This suppression technique is usually called interferometric surface-wave suppression.

In previous studies, the interferometric surface-wave suppression was applied in a non-recursive way on the data. Halliday et al. (2010) demonstrated its effectiveness in the context of hydrocarbon exploration, while Konstantaki et al. (2015) and Liu et al. (2018) showcased its utility for near-surface applications. Moreover, Balestrini et al. (2020) demonstrated its application for deep mineral explorations. Here, we suggest a new approach using the first output of the interferometric surface-wave suppression for more iterations. We term this technique "Recursive Interferometric Surface-wave Suppression" (RISS). This technique aims to enhance the efficacy of the data-driven surface-wave sup-

pression through an iterative procedures.

In this study, we demonstrate RISS on a 2D reflection dataset acquired in Scheemda, Groningen province, the Netherlands. By using RISS, we aim to enhance the visualisation of reflections, which can provide clearer images of the subsurface structures and enhance the overall interpretation of the seismic data. Such advancements are particularly critical for Groningen, where gas production has resulted in induced seismicity since 1963 (Muntendam-Bos et al., 2022). We evaluate the RISS results in comparison with those from other techniques such as time muting and f-k filtering.

Below, we first present in Section 2 the methodology of RISS. This will be followed by a description of the seismic data acquisition in Section 3, the results in Section 4, and then a discussion and the conclusions.

## 2. Methodology

In our proposed approach, SI is employed first to retrieve the dominant surface waves. The retrieved surface-wave energy is subsequently adaptively subtracted from the dataset. Following this, the obtained data is utilised to iterate through these two steps, contributing to the improvement of the reflection resolution. This section outlines the implementation of RISS.

### 2.1 Surface-wave retrieval by seismic interferometry

SI refers to the method of retrieving new seismic responses, for example between two receivers, using most commonly cross-correlation, as if there were a source at one of the receiver locations (Wapenaar & Fokkema, 2006; Wapenaar et al., 2010). In an active-source survey, this process is usually achieved by cross-correlating the recordings at the two receivers and then stacking the virtual traces over all available active sources (Halliday & Curtis, 2008). So, the retrieved response between two receivers at positions  $\mathbf{x}_A$  and  $\mathbf{x}_B$  can be expressed in the frequency domain, as described by Halliday et al. (2007):

$$\hat{G}^*(\mathbf{x}_B, \mathbf{x}_A, \omega) + \hat{G}(\mathbf{x}_B, \mathbf{x}_A, \omega) \propto \sum_{n=1}^N \hat{G}^*(\mathbf{x}_A, x_n, \omega) \hat{G}(\mathbf{x}_B, x_n, \omega), \quad (1)$$

where  $\hat{G}(\mathbf{x}_B, x_n, \omega)$  is the frequency-domain response of a recording at receiver  $\mathbf{x}_B$  and  $\hat{G}(\mathbf{x}_A, x_n, \omega)$  is the frequency-domain response of a recording at receiver  $\mathbf{x}_A$ , both from a source at  $x_n$  at the Earth's surface. The left-hand side of the equation represents the response between the two receivers at  $\mathbf{x}_A$  and  $\mathbf{x}_B$  at the surface, implying that we turn the receiver at  $\mathbf{x}_A$  into a virtual source. The symbol  $(*)$  denotes the complex conjugate in the frequency domain, while  $N$  represents the total number of active sources at the surface.

In a laterally homogeneous 2D medium, sources at points in line with the receivers contribute to the retrieval of direct surface-wave arrivals since they are all in the stationary-phase region, but only a few points are stationary to retrieve pseudo-physical (Löer et al., 2013) or ghost reflections (Draganov et al., 2012; Shirmohammadi et al., 2024) and scattered surface waves. This way, the results retrieved by SI will be dominated by surface waves (Balestrini et al., 2020).

Figure 1 shows a schematic representation of SI for retrieving direct arrivals, including surface waves. By correlating the recording at  $\mathbf{x}_B$  from the active source at  $\mathbf{x}$  in Figure 1a with a recording at  $\mathbf{x}_A$  in Figure 1c, the virtual response between  $\mathbf{x}_B$  and  $\mathbf{x}_A$  is retrieved, as illustrated by the purple arrow in Figure 1d at causal times (the causal part refers to times later than the zero time). Similarly, the virtual response between another receiver at  $\mathbf{x}_{B'}$  and a receiver at  $\mathbf{x}_A$  is retrieved by correlating the response at  $\mathbf{x}_{B'}$  in Figure 1b with  $\mathbf{x}_A$  in Figure 1c, as depicted by the orange arrow in Figure 1d at acausal times (the acausal part refers to times earlier than the zero time). In both cases, the receiver at  $\mathbf{x}_A$  acts as a virtual source as shown by the blue explosion in Figure 1d. We repeat this procedure for all active sources, e.g., as shown in Figure 1e for another active source at  $\mathbf{x}'$ . Finally, the Green's function and its time-reversal between the virtual source at  $\mathbf{x}_A$  and other receivers at  $\mathbf{x}_B$ ,  $\mathbf{x}_{B'}$ , and  $\mathbf{x}_{B''}$  are retrieved by stacking all virtual responses such as those shown in Figures 1d and 1e.

When we want to apply this technique to a field dataset, there are certain issues that need to be addressed in order to improve the resolution of the retrieved responses.

First, we aim to retrieve the direct surface waves with SI. So, it is required that all receivers be considered on the same side of the active source, e.g, for an active source

at  $\mathbf{x}$ , we correlate the response for receivers  $\mathbf{x}_B$  and  $\mathbf{x}_{B'}$  located on the same side as the virtual source at  $\mathbf{x}_A$ , as shown in Figures 1a, b, and c. In the same way, for an active source at  $\mathbf{x}'$ , we consider all receivers because they are on the same side as the virtual source at  $\mathbf{x}_A$ , as shown in Figure 1e. This condition is dictated by the theory of SI by cross-correlation, which states that the sources should surround the receivers, i.e., there must not be sources between the receivers involved in the correlation process.

Second, in the case of isotropic illumination of the receivers, a time-symmetric response between the receivers is obtained, as shown in equation 1. Consequently, one could sum the causal and the time-reversed acausal parts of the correlated panels to improve the signal-to-noise ratio. However, in practical situations, when the illumination is not homogeneous from all sides for each pair of receivers, then parts of the response can be retrieved at acausal times and other parts at causal times. Therefore, to enhance the quality of our retrieved responses, we meticulously assess the positions of virtual source-receiver pairs and active sources. Subsequently, we opt to select either the causal or time-reversed acausal part of the correlation panel.

Considering the conditions of one-sided distribution of receivers and causality, we limit ourselves to a minimum number of traces for stacking. To maintain a high signal-to-noise ratio, we stack traces only when we have at least half the number of all active sources. We can summarise this as follows:

$$trace \begin{cases} \text{causal part, if } m > N/2 \text{ with } \mathbf{x} < \mathbf{x}_A < \mathbf{x}_B, \text{ or } \mathbf{x} > \mathbf{x}_A > \mathbf{x}_B, \text{ or } \mathbf{x}_A = \mathbf{x}_B \\ \text{time-reversed acausal, if } m > N/2 \text{ with } \mathbf{x} < \mathbf{x}_B < \mathbf{x}_A, \text{ or } \mathbf{x} > \mathbf{x}_B > \mathbf{x}_A. \end{cases}$$

Here,  $\mathbf{x}$  is the position of the active sources,  $\mathbf{x}_A$  is the position of the virtual source,  $\mathbf{x}_B$  is the position of the receiver, and  $m$  is a number of active sources for stacking which should be higher than half the total number of active sources ( $N$ ). For instance, as illustrated in Figure 1d, for the receiver at  $\mathbf{x}_{B'}$  on the left side of the virtual source at  $\mathbf{x}_A$ , we consider the acausal part, as indicated by the orange arrow. Similarly, for a receiver at  $\mathbf{x}_B$ , we consider the causal part, indicated by the purple arrow. Furthermore, as depicted in Figure 1e, for the receiver at  $\mathbf{x}_B$  on the right side of the virtual source at  $\mathbf{x}_A$ , we consider the acausal part, and for other receivers at  $\mathbf{x}_{B'}$  and  $\mathbf{x}_{B''}$ , we consider the

causal part, as shown by the purple arrows. Considering the above factors, we retrieve 139  
the virtual common-source gather for all receivers. 140

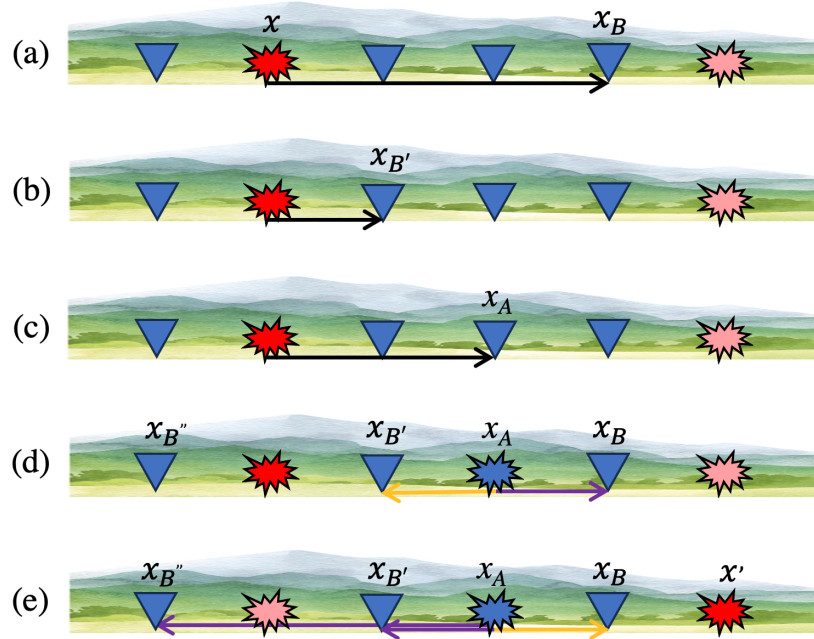


Figure 1: Schematic representation of seismic interferometry for retrieving surface waves. (a), (b), and (c) The surface wave recorded at  $x_B$ ,  $x_{B'}$ , and  $x_A$  from the active source at  $x$ , respectively. (d) The result of correlating the response at  $x_A$  with other receivers, and thus turning  $x_A$  into a virtual source. (e) Same as (d) but for the active source at  $x'$ . The black arrows indicate the surface waves, while the orange and purple arrows represent the outcomes of correlation, considering the causal and acausal parts, respectively.

## 2.2 Adaptive subtraction 141

When each source position in an active-source survey is in close proximity to a receiver 142  
position, we are able to identify a corresponding retrieved virtual common-source gather 143  
with estimated dominant surface waves for each active source–virtual source pair. These 144  
estimates can then be adaptively subtracted from the complete responses of the active 145  
source pair (Halliday & Curtis, 2008, Halliday et al., 2010, Konstantaki et al., 2015). 146

Figure 2 shows the basic principle of adaptive subtraction. Figure 2a illustrates schem- 147  
atically a simple seismic trace that consists of a primary reflection at 100 ms, shown in 148  
black, and surface waves at 300 ms, 350 ms, and 400 ms in blue. Figure 2b shows the 149  
result of SI, which contains surface waves. By minimising the difference between Fig- 150  
ure 2b and Figure 2a, the surface waves in Figure 2a can be suppressed partly, as shown 151  
in Figure 2c. The minimisation is done by estimating a shaping filter  $\mathbf{f}$  that can minimise 152

the following objective function (Liu et al., 2018; Balestrini et al., 2020): 153

$$\min_{\mathbf{f}} \|D - \mathbf{f}D_{SW}\|^2, \quad (2)$$

where  $D$  is the field dataset with surface waves and  $D_{SW}$  are the surface waves retrieved by 154  
SI using the field dataset. The vertical double bars  $\|\cdot\|^2$  represent the L2 norm. Equation 2 155  
is solved using an iterative least-squares fit (Verschuur et al., 1992). More details can be 156  
found in Alá'i & Verschuur (2003) and Verschuur (2013). The multiplication between the 157  
 $\mathbf{f}$  and  $D_{SW}$  is directly subtracted from  $D$ , giving  $D_{ref}$  which represents the data after 158  
surface-wave suppression as 159

$$D_{ref} = D - \mathbf{f}D_{SW}. \quad (3)$$

As illustrated in Figure 2c, the data after adaptive subtraction may still contain surface 160  
waves due to, for example, errors in estimating higher modes of surface waves. Therefore, 161  
we suggest repeating the same step of SI and adaptive subtraction but now using the 162  
output of the first adaptive subtraction, represented here as Figure 2c, as input for SI. 163  
We estimate surface waves from SI, as shown in Figure 2d, and then adaptively subtract 164  
them from Figure 2c. Figure 2e shows the final result, whereby repeating these steps, 165  
we increase our chances of suppressing all the surface-wave energy and preserving weak 166  
reflections (the black event). We call this technique RISS. Note, that RISS can be applied 167  
for one iteration or multiple iterations. 168

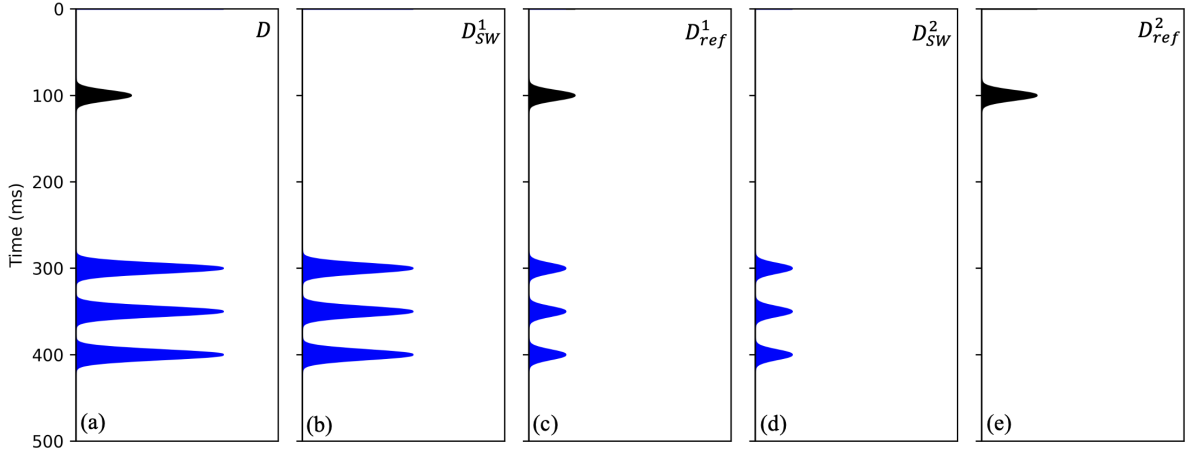


Figure 2: Schematic representation of Recursive Interferometric Surface-wave Suppression (RISS). (a) A seismic trace  $D$  with a primary reflection in black and surface waves in blue, (b)  $D_{SW}^1$  is a result of SI, (c)  $D_{ref}^1$  is the trace after the first iteration of RISS, (d)  $D_{SW}^2$  is a result of SI when using  $D_{ref}^1$  in (c) as input, (e)  $D_{ref}^2$  after a second iteration of RISS.

### 3. Seismic data acquisition

169

We acquired a 2D seismic reflection data close to the town of Scheemda in the Groningen 170  
 province of the Netherlands in 2022. Figures 3a and 3b show the location of the site and 171  
 the geometry of the reflection line, respectively. We employed an electric linear motor 172  
 system (LMS) seismic vibrator (Noorlandt et al., 2015) as a source, with a spacing of 2 173  
 m (red stars in Figure 3b), and 601 three-component geophone nodes as receivers (the 174  
 circles in Figure 3b), with a spacing of 1 m. The acquisition parameters are summarised 175  
 in Table 1. 176

For this survey, we used the electrical vibrator in the S-wave mode and oriented in the 177  
 crossline direction. We then used the data recorded by the crossline horizontal component 178  
 of the geophones. Because of the orientation of the sources and the receivers, and assuming 179  
 no scattering from the crossline direction, the horizontally polarised S-waves (SH-waves) 180  
 we record are generally decoupled from the compressional and vertically polarised S-waves. 181



Table 1: Acquisition parameters

Parameter	Value
Number of source positions	151
Source spacing	2 m
First source position	150.5
Last source position	450.5
Number of receiver positions per source	601
Receiver spacing	1 m
First receiver position	0 m
Frequency range of the sweep	8-250 Hz

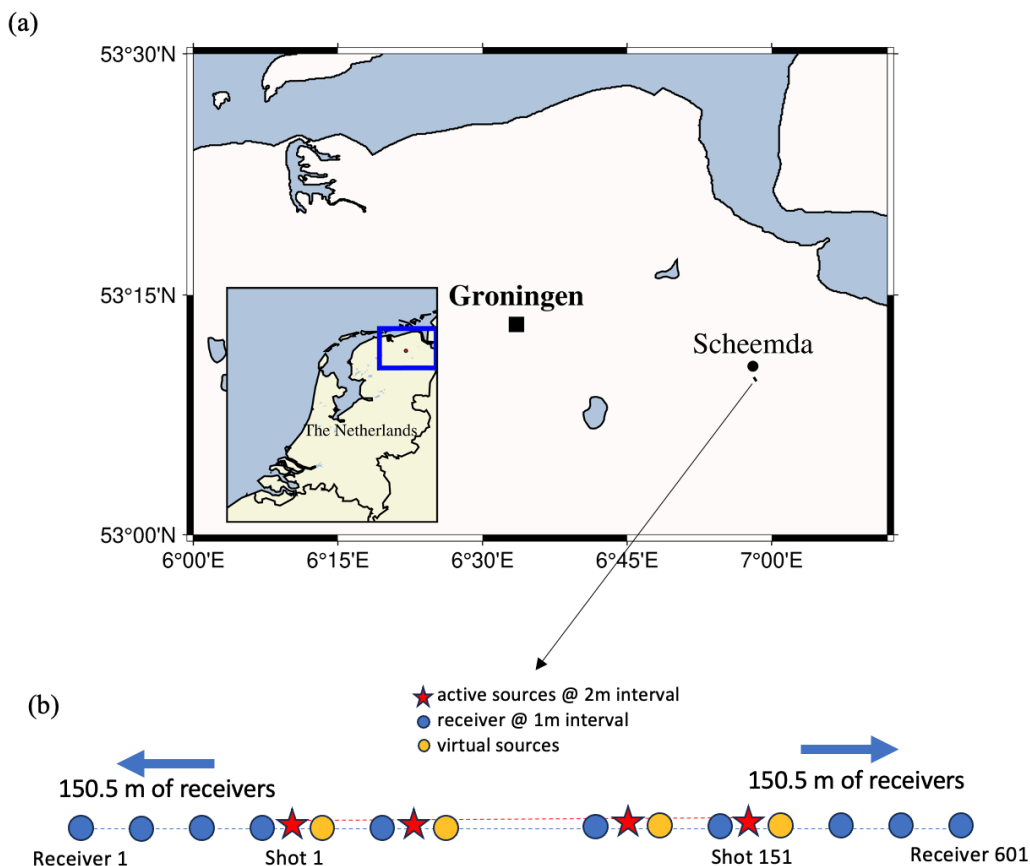


Figure 3: (a) Location of the test site, and (b) the geometry of the seismic line. The red stars represent active sources, the blue circles represent receivers, and the orange circles represent receivers which act as virtual sources for applying the RISS.

## 4. Results

182

The primary aim of this study is to examine the effectiveness of the RISS technique. 183

We apply the technique to common-source gathers of the field data, as introduced in 184

Section 3. The data processing involves several steps. Figure 4 shows a flowchart of these 185

steps for the RISS, but also other techniques such as f-k filtering and surgical muting for 186

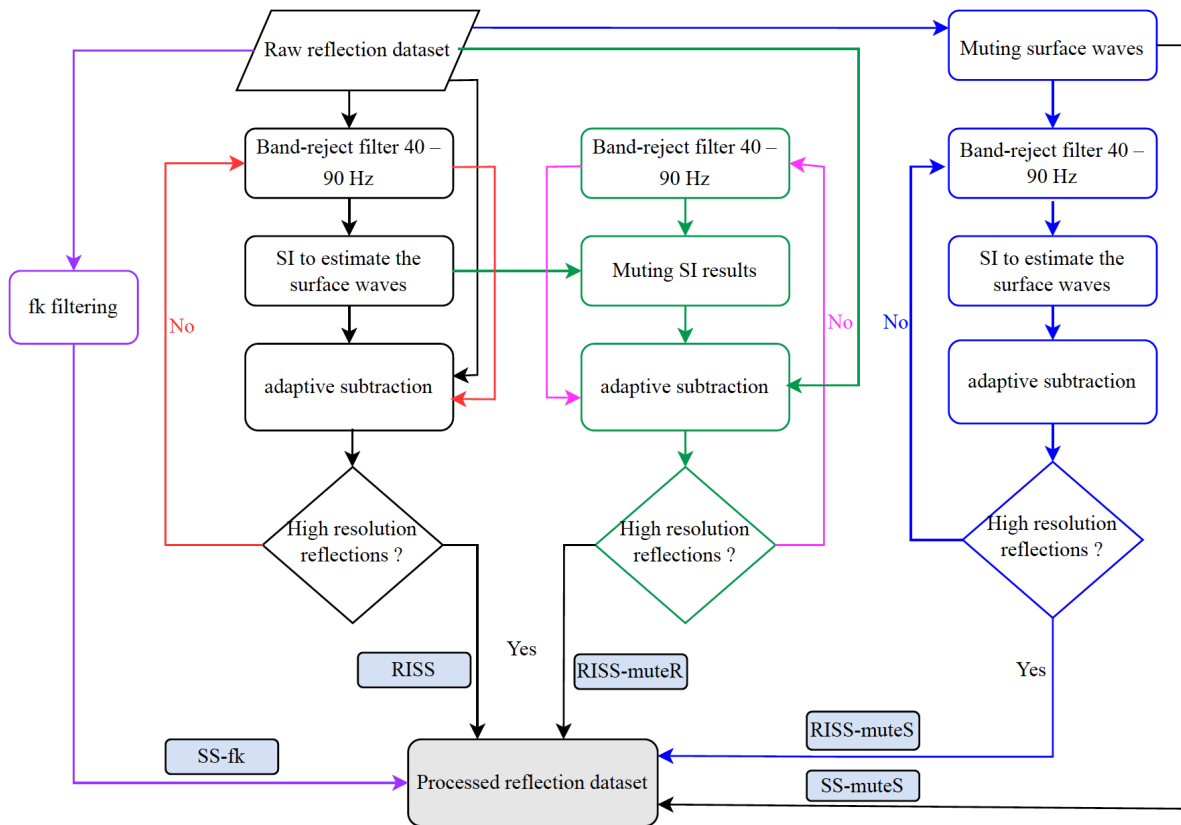


Figure 4: Flowchart for applying surface-wave suppression. RISS represents steps for the Recursive Interferometric Surface-wave Suppression, the RISS-muteR is the same as RISS but using muted SI results, the RISS-muteS is the same as RISS but using time-muted reflection dataset as input for SI, SS-fk represents surface-wave suppression using f-k filtering, SS-muteS represents surface-wave suppression using time-muted reflection dataset.

As shown in Figure 4, first we apply a band-reject filter between 40 Hz and 90 Hz 188  
to all active common-source gathers. The main idea is to reject frequencies that might 189  
contain reflections but not surface waves so that the SI result would predominantly contain 190  
retrieved surface waves. We select these frequencies based on the power spectrum of the 191  
common-source gathers. We then apply SI as described in section 2.1 by selecting each 192  
receiver close to an active source to turn it into a virtual source, as shown by the orange 193  
circles in Figure 3b. 194

Next, we adaptively subtract the result retrieved by SI for each virtual source from the 195  
original active-source data which is closest to the virtual source to suppress the surface 196  
waves, using an estimated matching filter as described in section 2.2. 197

It is essential to determine carefully the key parameters for the matching filter: time 198  
window, space window, and filter length. We choose 20 traces for the space window and 199

0.2 s for time time window, with a filter length of 0.05 s. We apply the same steps for 200  
all virtual sources. Figure 5a shows an example of the original common-source gather in 201  
the time domain, while Figure 5b shows the same gather after RISS with one iteration, 202  
for an active source located at lateral position 320.5 m, i.e., after the SI interferometric 203  
suppression as applied till now. 204

As discussed in Section 2, we propose to apply the RISS for more than one iteration 205  
which means we use the data after the first iteration of the RISS as input for applying SI. 206  
Then, we repeat all steps i.e., band-reject filtering, SI, and adaptive subtraction. Note 207  
that these steps are shown as "RISS" in the flowchart in Figure 4. 208

Figure 5c shows the same gather as in Figures 5a and 5b but after the second iteration 209  
of the RISS. Comparing these three results, we observe that a large part of the surface- 210  
wave energy is suppressed in Figure 5c, as shown by the white arrows. Figures 5d-5f 211  
show the f-k spectra of the common-source gathers in Figures 5a-5c, respectively. The 212  
surface-wave energy appears as linear events in the f-k domain, as indicated by the blue 213  
arrows; they are largely suppressed from the data after the RISS with two iterations, as 214  
can be observed in Figure 5f. 215

Figure 6 shows another example for a common-source gather for a source located at a 216  
lateral position of 430.5 m, where we also observe significant suppression of the surface- 217  
wave energy in both the space-time and f-k domain. 218

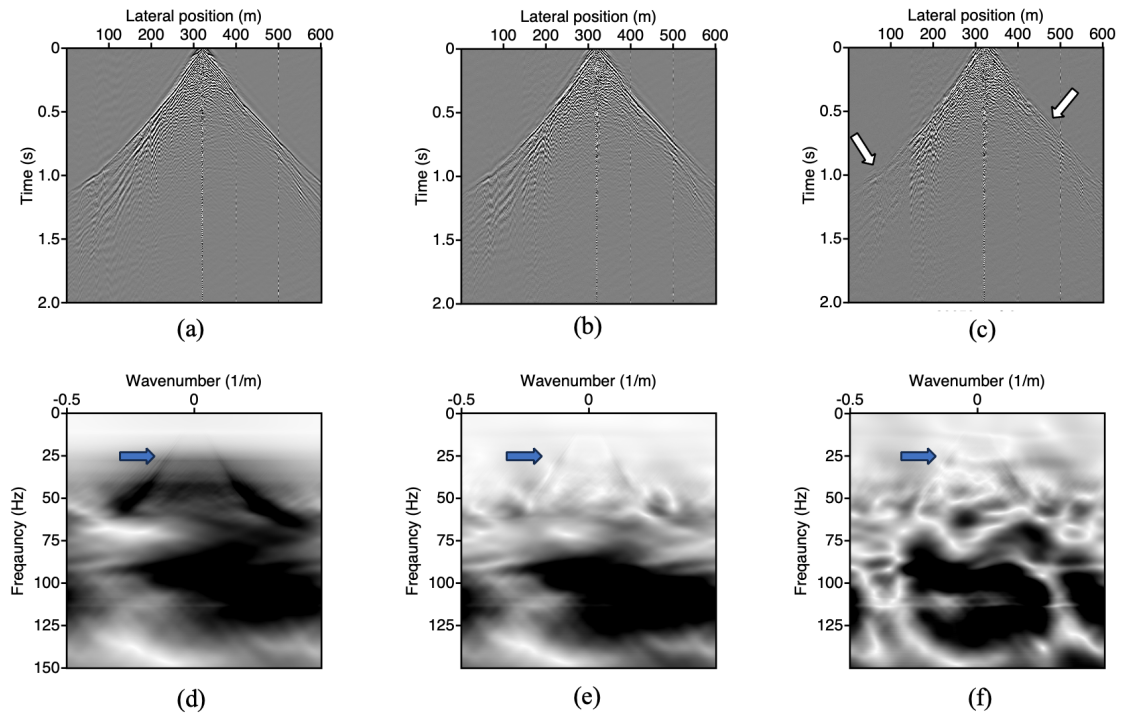


Figure 5: (a) A common-source gather for a source located at lateral position 320.5 m, (b) same common-source gather after the first iteration of the RISS, (c) same common-source gather after the second RISS iteration; (d), (e) and (f) same as (a), (b), and (c), respectively, but in the f-k domain. White arrows point to suppressed surface waves in the space-time domain and blue arrows point to surface-wave energy in the f-k domain.

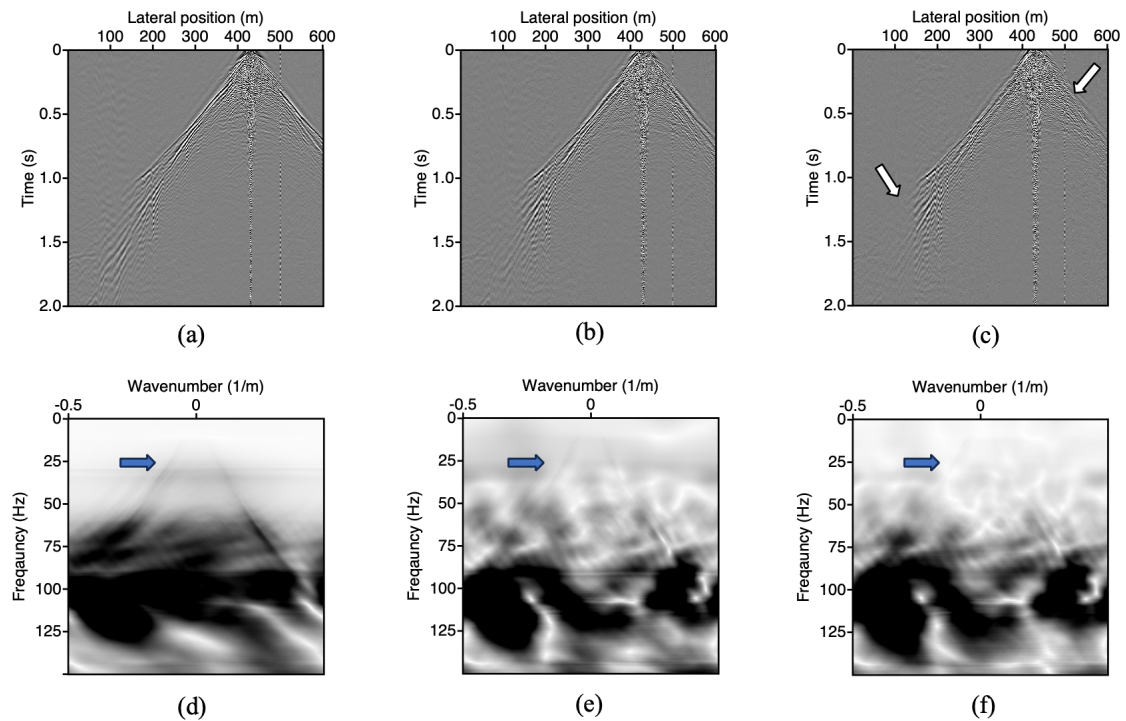


Figure 6: Same as Figure 5 but for a source at a lateral position 430.5 m.

As depicted in Figures 5c and 6c, we successfully suppress the surface waves. However, it appears that some deeper reflections are also suppressed in the process (the red pointers in Figures 7a and 7d). This shows that applying a simple band-reject filter and relying on having less sources in the stationary-phase regions contributing to retrieval of reflections might not guarantee that the retrieved reflection energy is absent or even weak. To preserve these reflections in the original common-source gathers, we apply a bottom muting to the virtual-common-source gathers retrieved from SI before adaptive subtraction, which we label as "RISS-muteR" in the flowchart in Figure 4. Figures 7b and 7e show the common-source gather after applying the RISS using the muted SI results for two active sources located at 320.5 m and 430.5 m, respectively. In comparison with Figures 7a and 7d, which show the same common-source gather after RISS, we observe clearer deeper reflections as marked by the red arrows.

By examining the common-source gathers, we observe that it is feasible to suppress some parts of the surface waves through surgical muting, which is a common approach. Therefore, prior to applying the RISS, we can also surgically mute the prominent surface waves. We label this procedure as "RISS-muteS" in the flowchart in Figure 4. Figures 7c and 7f show the common-source gather after the RISS-muteS. Although we enhance the resolution of some reflections, we still seems to have some strong surface-wave energy in comparison with the results in Figures 7a and 7d as highlighted by the blue ellipses. This observation underscores the fact that by suppressing the surface waves in common-source gathers before the RISS, it becomes challenging to retrieve the surface waves by SI.

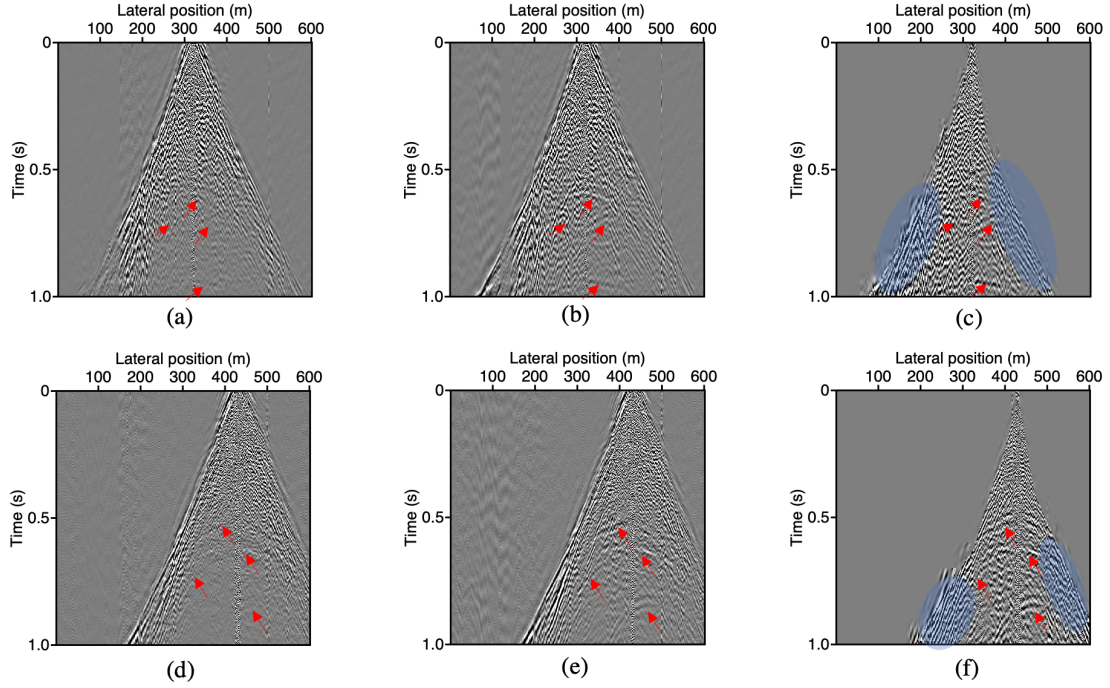


Figure 7: (a) A common-source gather for a source located at lateral position 320.5 m after the RISS, (b) same common-source gather after the RISS-muteR, (c) same common-source gather after the RISS-muteS, (d), (e) and (f) same as (a), (b), and (c), respectively, but for a source located at a lateral position of 430.5 m. Red arrows point to enhanced reflections, while the blue ellipses highlight parts of the surface waves.

After the suppression of the surface waves, we apply conventional seismic processing 240  
to obtain preliminary unmigrated stacked sections for a better comparison between the 241  
result of the RISS and the conventional suppression techniques. A summary of these 242  
steps is presented in Table 2. We first apply bandpass filtering, amplitude correction for 243  
absorption effects and geometrical spreading, and then automatic gain control (AGC) for 244  
amplitude balancing for visualization purposes. 245

Next, we sort the data into common-midpoint (CMP) gathers (CMP spacing 0.5 m). 246  
As expected, the CMP fold increases towards the center of the line where better illumin- 247  
ation is achieved. We then apply normal moveOut (NMO) correction using a constant 248  
velocity of 350 m/s, and finally, we stack the CMP gathers. The constant velocity of 249  
350 m/s is selected based on a comparison of the stacked sections with different velocity 250  
values, as this velocity yields better results. Figure 8 shows the preliminary, unmigrated 251  
stacked section between 151.25 m and 450.25 m lateral distances for the five approaches 252  
for surface-wave suppression as illustrated in Figure 4. Since we know that the most sig- 253  
nificant influence of the surface waves is related to the shallowest part of the subsurface, 254

we focus our attention to these parts, specifically 400-800 ms. 255

Figure 8a shows the time section obtained after suppressing the surface waves using 256  
surgical muting, as indicated by SS-muteS in the flowchart. We use this figure as a 257  
reference because this suppression approach is standard and experienced data processors 258  
generally achieve good results. This result is comparable with results from other studies, 259  
e.g., that in Kruiver et al. (2017). Figure 8b shows the time section using the result 260  
after the second iteration of the RISS. In comparison with the reference time section, it 261  
is obvious that some of the expected reflectors are suppressed as shown by the light blue, 262  
red, and green arrows. 263

To address this issue, we use the RISS-muteR as explained above. Figure 8c illustrates 264  
the time section obtained after the application of this technique. In comparison with the 265  
reference in Figure 8a, we retrieve all reflectors, as indicated by the light blue, red, and 266  
green arrows. Moreover, some dome-like structures are now interpretable as highlighted 267  
by the red curves. 268

Figure 8d shows the time section after applying RISS-muteS. Comparing this image to 269  
the images in Figures 8a, 8c, we see that the lateral continuity of the reflectors is worse, 270  
e.g., inside the blue ellipse, while the general character on the left part of the image 271  
has become lower in frequency, which might point to the presence of left-over dominant 272  
surface-wave energy. Figure 8e shows the time section obtained after suppression of the 273  
surface waves by f-k filtering (SS-fk), which is another common surface-wave suppression 274  
technique. Comparing this image to the images in Figures 8a, 8c, we see that the result 275  
in Figure 8e is generally of good quality. The reflector indicated by the green arrow even 276  
appears laterally more continuous than in Figures 8a, 8c. However, other reflectors are 277  
less clear, e.g., the one indicated by the blue arrow or those on in the left part of the 278  
image earlier than 600 ms (see specifically inside the blue ellipse). 279

Based on this comparison, it appears that the best image the one in Figure 8c, i.e., 280  
after application of RISS-muteR, because of its clarity but also because the surface-wave 281  
suppression is data-driven. 282

Table 2: Summary of seismic processing steps.

Step	Instruction
1	Band-pass filter between 30-100 Hz
2	Amplitude corrections
3	Automatic gain control (AGC)
4	Time muting
5	Normal moveout (NMO) correction
6	Common midpoint/ensemble stack

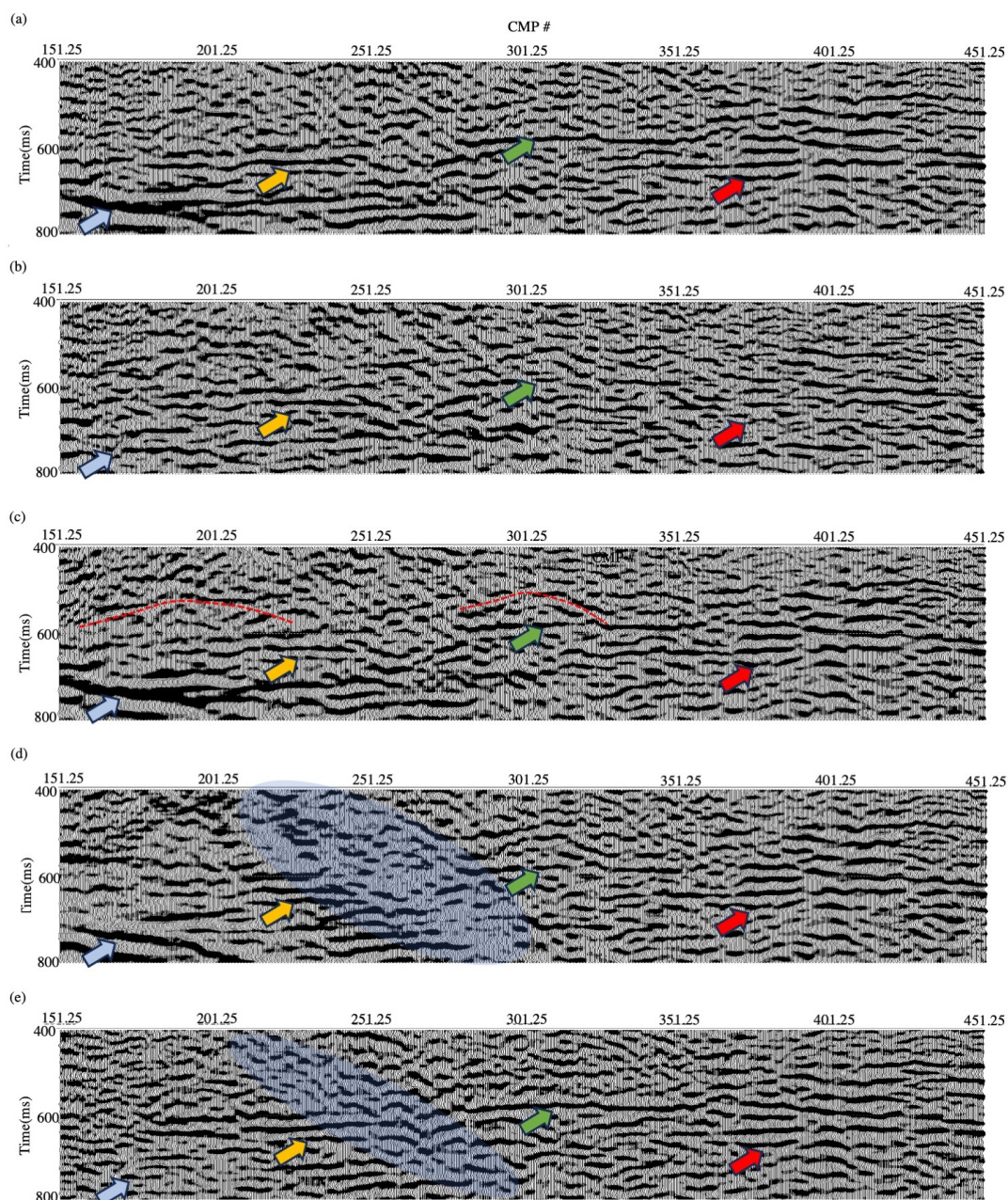


Figure 8: Preliminary, unmigrated stacked section using a constant velocity of 350 m/s zoomed in 400-800 ms, (a) using the reflection dataset after surgical muting of surface waves ("SS-muteS"), (b) after the secon iteration of the RISS, (c) after the RISS using the muted SI results (RISS-muteR), (d) using the data as in (a) but after the RISS ("RISS-muteS"), (e) after f-k filtering ("SS-fk"). The colored arrows point to strong reflectors and the blue ellipses highlight artefacts.



To demonstrate the applicability of using SI for surface-wave suppression in imaging the shallow subsurface, we further investigate its use for the Marchenko-based isolation (Wapenaar & van IJsseldijk, 2021; van IJsseldijk et al., 2023). The Marchenko method can estimate Green's functions between the Earth's surface and arbitrary locations in the subsurface. These Green's functions are used to redatum wavefields to a deeper level in the subsurface (Slob et al., 2014; Wapenaar et al., 2014). The Marchenko method can also be used to isolate the response of a specific layer or package of layers, free from the influence of the overburden and underburden. The complete derivation of the Marchenko-based isolation is beyond the scope of this paper; however, a detailed description can be found in van IJsseldijk et al. (2023), van IJsseldijk et al. (2024). Moreover, a complete description of the application of the Marchenko-based isolation on the field dataset used in this study can be found in Shirmohammadi (2024).

We use the Marchenko-based isolation to eliminate the overburden and the underburden, and isolate the reflection from the target layer between 30 m and 270 m using the data after surgical muting of surface waves and the data after RISS-muteR. Figure 9a shows the stacked section using the regular reflection response after suppression of the surface waves using surgical muting, while Figures 9b and 9c show the stacked section using the reflection response after Marchenko-based isolation for overburden and underburden removal, using surgical muting for surface-wave suppression and RISS-muteR, respectively.

A comparison of these stacked section in Figure 9 suggests the potential elimination of the internal multiples originating from the overburden, down to 30 m using the Marchenko-based isolation. The shallow reflectors appear clearer and more continuous, as indicated by the color-coded arrows. But what we want to draw attention to is the effect of surface-wave suppression on these results. We observe enhanced reflections with a greater clarity of the stacked sections after RISS-muteR (Figure 9c), as exemplified by the events indicated by the white and green arrows. Moreover, there are fewer artefacts, likely from surface waves, as indicated by the black ellipse.

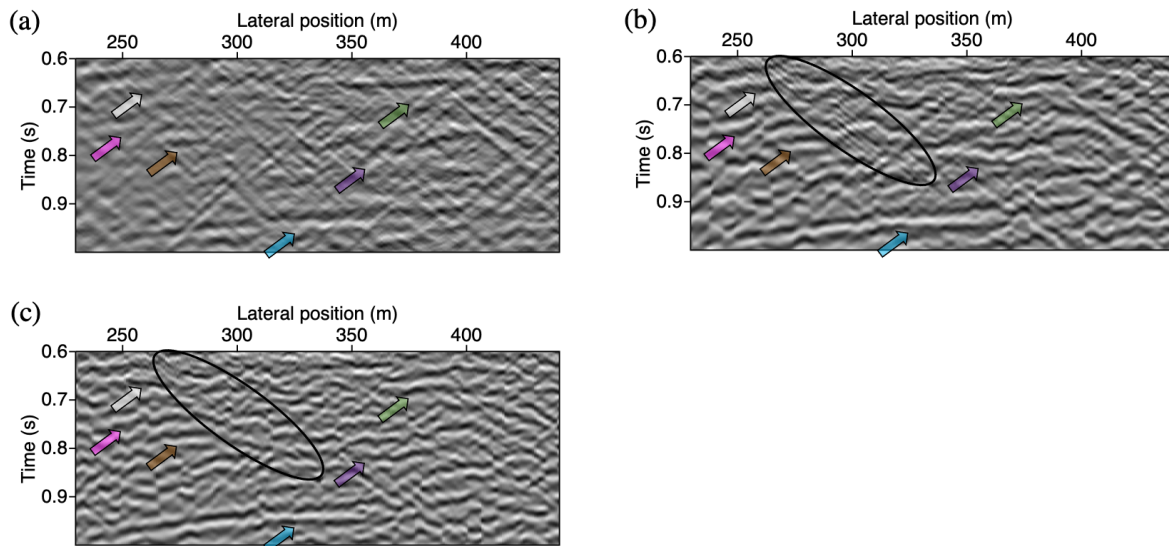


Figure 9: Stacked sections, zoomed in between 0.6 s and 1.0 s, obtained using (a) the regular reflection response after surgical muting of the surface waves, (b) the reflection response after Marchenko-based isolation for overburden and underburden removal after surgical muting of the surface waves, and (c) similar to (b) but using data after surface-wave suppression with RISS-muteR instead of surgical muting. The colour-coded arrows indicate reflectors. The black ellipse highlights potential artefacts from the surface waves that are suppressed in (c).

## 5. Discussion 311

We presented a comparison of different approaches for surface-wave suppression applied 312  
to the land seismic dataset acquired in Scheemda, Groningen province: surgical muting, 313  
f-k filtering, the RISS, the RISS-muteR, and the RISS-muteS. 314

From a comparison of the unmigrated time sections, we found that surgical muting 315  
seems convenient for removing surface waves in our dataset. However, this method does 316  
not adequately remove the surface-wave energy, as surface waves overlap with useful 317  
reflections and scattered arrivals. Additionally, weak reflections and scattered arrivals 318  
covered by surface waves might also be muted, as demonstrated earlier by Konstantaki et 319  
al. (2015). The other common technique for surface-wave suppression -f-k filtering- could 320  
cause more artefacts, as it is challenging to define the correct parameters for frequency and 321  
wavenumber windows for all common-source gathers. In contrast, the RISS technique can 322  
effectively suppress surface waves without prior information, as it is purely data-driven. 323

By comparing three approaches for the RISS, we found that the RISS using muted 324  
deeper reflections after retrieving the surface waves with SI yields the best results. RISS 325

with two iterations was sufficient to achieve the desired results for our dataset. However, 326  
for more than two iterations can be needed for other datasets. 327

For implementation of the RISS, we must determine the time, spacing window, and 328  
the filter length. We determined these parameters carefully by examining different values 329  
for them. Balestrini et al. (2020) demonstrated that changing the time and the space 330  
window size makes no significant differences. They also observed that increasing the filter 331  
length produces undesirable artefacts at earlier times. Defining a proper filter length can 332  
be indeed crucial for different datasets. 333

A comparison of the surface-wave dispersion curves obtained from the results of SI with 334  
active common-source gathers shows that the kinematics of the higher modes of surface 335  
waves cannot be accurately retrieved using SI, as depicted in Figure 10. Consequently, 336  
effective suppression of these higher modes poses a significant challenge. As highlighted 337  
by Halliday & Curtis (2008), modal separation is possibly a crucial step before applying SI 338  
to ensure the correct kinematic retrieval and consecutive suppression of the higher modes 339  
with minimal error. On the other hand, the RISS can help suppress the higher modes, as 340  
we have demonstrated here. This happens as, during each iteration, the strongest present 341  
surface-wave mode is retrieved and adaptively suppressed, which could effectively be seen 342  
as step-wise modal separation. 343

As described in the methodology section, we utilised the field dataset with surface 344  
waves for each active source as a reference, and for the virtual sources, the surface waves 345  
were retrieved using SI. In our study, we created at receiver locations as the virtual sources, 346  
which are positioned at 0.5 m from the active sources; this provides an appropriate dataset 347  
for applying this technique. However, using virtual sources located at greater distances 348  
from the active sources may result in incorrect estimations of the surface waves using SI. 349  
Therefore, we recommend using sources and receivers in close proximity of each other to 350  
ensure the accuracy of RISS. 351

Finally, besides the application of SI for surface-wave suppression, it is also possible 352  
to utilise SI for surface-wave retrieval at each receiver, which can be achieved by applying 353  
an extra step- a subtraction of the result of RISS from the original dataset, resulting in 354  
a virtual source gather with only surface waves at each receiver position. This approach 355

would be beneficial in cases where more sources are needed, such as for full-waveform inversion of surface waves.

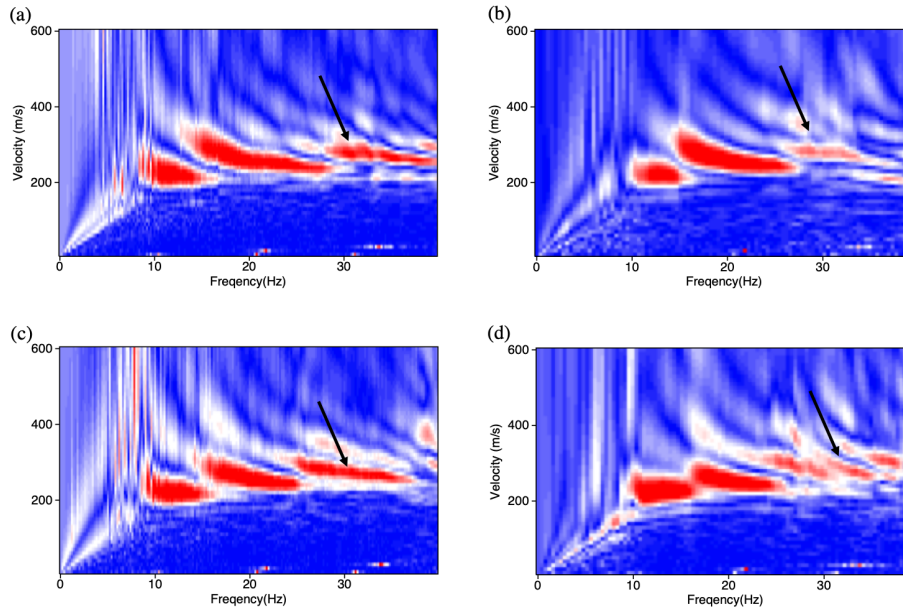


Figure 10: Dispersion curves (a) for an active source at 320.5 m, (b) the virtual source at 320 m, (c) same as (a) but for the active source at 430.5 m, and (d) same as (b) but for the virtual source at 430 m. The black arrows point to higher modes of surface waves.

## 6. Conclusion

We proposed recursive application of seismic interferometry (SI) for surface-wave suppression. We showcased our technique using a 2D reflection dataset acquired in Scheemda, Groningen province, the Netherlands. We applied SI to retrieve dominant surface waves between receivers while minimising the retrieved reflection energy. The retrieved dominant surface waves were then adaptively subtracted from the original data. We showed that applying these two steps two times, i.e., recursively, resulted in a fully data-driven effective suppression of the surface waves.

We compared stacked sections obtained through the recursive interferometric surface wave suppression with stacked sections where the surface waves were suppressed using f-k filtering and surgical muting. We found that the obtained time section after the second iteration of recursive interferometric surface-wave suppression yielded better results in terms of clearer and more continuous reflections, especially when the SI result was used

in which the retrieved reflection energy was minimised by bottom muting before SI. This 371  
technique can be effective for enhancing the resolution of the seismic reflection events for 372  
subsurface investigations or alternatively for obtaining surface waves free from body-wave 373  
reflections. 374

## 7. Acknowledgement 375

We acknowledge the use of computational resources provided by the DelftBlue supercom- 376  
puter at the Delft High Performance Computing Centre (<https://www.tudelft.nl/dhpc>) 377  
and thank Seismic Mechatronics for allowing us to use their vibrator source during field- 378  
work. (<https://seismic-mechatronics.com/>) 379

This research is funded by NWO Science domain (NWO-ENW), project DEEP.NL.2018.048 380  
and the reflection dataset was acquired by funding from the European Research Council 381  
(ERC) under the European Union’s Horizon 2020 research and innovation programme 382  
(Grant Agreement No. 742703) and OYO Corporation, Japan: OYO-TUD Research 383  
Collaboration (Project code C25B74). 384

## 8. Data availability 385

The field reflection dataset used in this study is available in the 4TU.ResearchData re- 386  
pository at <https://doi.org/10.4121/a8553b7e-82ae-4e9b-bc54-2a6b9ca6063c>. 387

The codes are also accessible in the 4TU.ResearchData repository at <https://doi.org/10.4121/6271c7d3-f931-49e9-b2b0-2d05eef7d3ae>. 388  
389

## References 390

Alá’i, R., & Verschuur, D. (2003). Simultaneous adaptive least-squares subtraction of 391  
multiples. *European Association of Geoscientists & Engineers*, Article cp-6-00176, 392  
1–4. <https://doi.org/10.3997/2214-4609-pdb.6.P193> 393

- Balestrini, F., Draganov, D., Malehmir, A., Marsden, P., & Ghose, R. (2020). Improved target illumination at Ludvika mines of Sweden through seismic-interferometric surface-wave suppression. *Geophysical Prospecting*, 68(1), 200–213. <https://doi.org/10.1111/1365-2478.12890>
- Dong, S., He, R., & Schuster, G. T. (2006). Interferometric prediction and least squares subtraction of surface waves. *SEG Technical Program Expanded Abstracts 2006*, 2783–2786. <https://doi.org/10.1190/1.2370102>
- Draganov, D., Heller, K., & Ghose, R. (2012). Monitoring CO2 storage using ghost reflections retrieved from seismic interferometry. *International Journal of Greenhouse Gas Control*, 11(SUPPL), S35–S46. <https://doi.org/10.1016/j.ijggc.2012.07.026>
- Halliday, D., & Curtis, A. (2008). Seismic interferometry, surface waves and source distribution. *Geophysical Journal International*, 175, 1067–1087. <https://doi.org/10.1111/j.1365-246X.2008.03918.x>
- Halliday, D., Curtis, A., Robertsson, J. O., & van Manen, D. J. (2007). Interferometric surface-wave isolation and removal. *Geophysics*, 72(5), A69–A73. <https://doi.org/10.1190/1.2761967>
- Halliday, D., Curtis, A., Vermeer, P., Strobbia, C., Glushchenko, A., van Manen, D.-J., & Robertsson, J. O. (2010). Interferometric ground-roll removal: Attenuation of scattered surface waves in single-sensor data. *Geophysics*, 75(2), SA15–SA25. <https://doi.org/10.1190/1.3360948>
- Konstantaki, L., Draganov, D., Ghose, R., & Heimovaara, T. (2015). Seismic interferometry as a tool for improved imaging of the heterogeneities in the body of a landfill. *Journal of Applied Geophysics*, 122, 28–39. <https://doi.org/10.1016/j.jappgeo.2015.08.008>
- Kruiver, P. P., van Dedem, E., Romijn, R., de Lange, G., Korff, M., Stafleu, J., Gunnink, J. L., Rodriguez-Marek, A., Bommer, J. J., van Elk, J., & Doornhof, D. (2017). An integrated shear-wave velocity model for the Groningen gas field, the Netherlands. *Bulletin of Earthquake Engineering*, 15, 3555–3580. <http://link.springer.com/10.1007/s10518-017-0105-y>

- Liu, J., Draganov, D., & Ghose, R. (2018). Seismic interferometry facilitating the imaging of shallow shear-wave reflections hidden beneath surface waves. *Near Surface Geophysics*, 16(3), 372–382. <https://doi.org/10.3997/1873-0604.2018013>
- Löer, K., Meles, G. A., Curtis, A., & Vasconcelos, I. (2013). Diffracted and pseudo-physical waves from spatially limited arrays using source-receiver interferometry (SRI). *Geophysical Journal International*, 196(2), 1043–1059. <https://doi.org/10.1093/gji/ggt435>
- Muntendam-Bos, A. G., Hoedeman, G., Polychronopoulou, K., Draganov, D., Weemstra, C., van der Zee, W., Bakker, R. R., & Roest, H. (2022). An overview of induced seismicity in the Netherlands. *Geologie en Mijnbouw/Netherlands Journal of Geosciences*, 101(2), 1–20. <https://doi.org/10.1017/njg.2021.14>
- Noorlandt, R., Drijkoningen, G., Dams, J., & Jenneskens, R. (2015). A seismic vertical vibrator driven by linear synchronous motors. *Geophysics*, 80(2), EN57–EN67. <https://doi.org/10.1190/GEO2014-0295.1>
- Shirmohammadi, F. (2024). *Layer-specific imaging and monitoring using seismic interferometry and the Marchenko method* [Ph.D. thesis]. Delft University of Technology [Submitted].
- Shirmohammadi, F., Draganov, D., Veltmeijer, A., Naderloo, M., & Barnhoorn, A. (2024). Feasibility of reservoir monitoring in the Groningen gas field using ghost reflections from seismic interferometry. *Geophysical Journal International*, 237(2), 1018–1029. <https://doi.org/10.1093/gji/ggae099>
- Slob, E., Wapenaar, K., Broggini, F., & Snieder, R. (2014). Seismic reflector imaging using internal multiples with Marchenko-type equations. *Geophysics*, 79(2), S63–S76. <https://doi.org/10.1190/GEO2013-0095.1>
- van IJsseldijk, J., Brackenhoff, J., Thorbecke, J., & Wapenaar, K. (2024). Time-lapse applications of the Marchenko method on the troll field. *Geophysical Prospecting*, 72, 1026–1036. <https://doi.org/https://doi.org/10.1111/1365-2478.13463>
- van IJsseldijk, J., Neut, J. V. D., Thorbecke, J., & Wapenaar, K. (2023). Extracting small time-lapse travelttime changes in a reservoir using primaries and internal multiples

- after Marchenko-based target zone isolation. *Geophysics*, 88(2), R135–R143. <https://doi.org/10.1190/geo2022-0227.1>
- Verschuur, D. J., Berkhout, A. J., & Wapenaar, C. P. A. (1992). Adaptive surface-related multiple elimination. *Geophysics*, 57(9), 1166–1177. <https://doi.org/10.1190/1.1443330>
- Verschuur, D. (2013). *Seismic multiple removal techniques - past, present and future*. European Association of Geoscientists & Engineers (EAGE). <https://app.knovel.com/hotlink/toc/id:kpSMRTPPF2/seismic-multiple-removal/seismic-multiple-removal>
- Wapenaar, K., & van IJsseldijk, J. (2021). Employing internal multiples in time-lapse seismic monitoring, using the Marchenko method. *82nd EAGE Conference and Exhibition 2021*, 1–5. <https://doi.org/10.3997/2214-4609.202011576>
- Wapenaar, K., Draganov, D., Snieder, R., Campman, X., & Verdel, A. (2010). Tutorial on seismic interferometry: Part 1 — basic principles and applications. *Geophysics*, 75, 75A195–75A209. <https://doi.org/10.1190/1.3457445>
- Wapenaar, K., & Fokkema, J. (2006). Green’s function representations for seismic interferometry. *Geophysics*, 71(4), SI33–SI46. <https://doi.org/10.1190/1.2213955>
- Wapenaar, K., Thorbecke, J., Van der Neut, J., Brogгинi, F., Slob, E., & Snieder, R. (2014). Marchenko imaging. *Geophysics*, 79(3), WA39–WA57. <https://doi.org/10.1190/GEO2013-0302.1>
- Yilmaz, Ö. (2001). *Seismic data analysis*. Society of Exploration Geophysicists. <https://doi.org/10.1190/1.9781560801580>